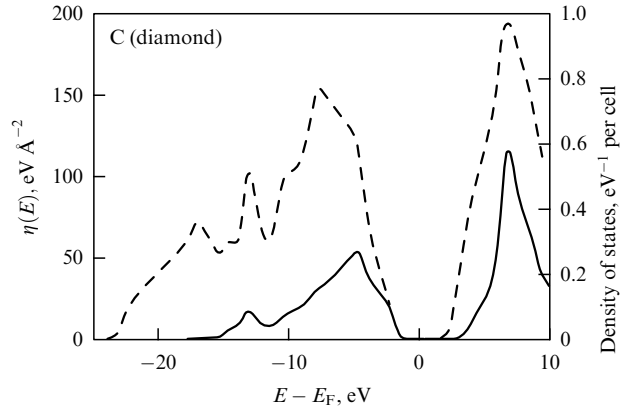

Figure 3. Electron-state density (dashed line) and the Hopfield parameter for diamond (solid line) (borrowed from [18]).

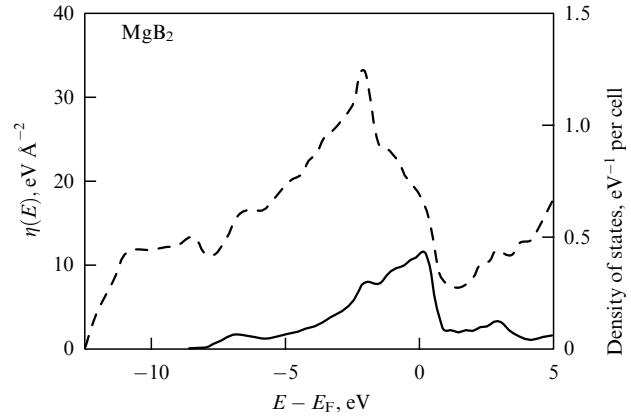

Figure 4. The density of electron states (dashed line) and the Hopfield parameter for MgB_2 (solid line) (borrowed from [18]).

strong covalent bonds. The authors of [17, 18] used another approach to the problem of high-temperature superconductivity in EPI systems. They rewrote $N(0)\langle I_i^2\rangle$ not only for energies at the Fermi surface but also for any energies using the Hopfield parameter η,

$$\eta_i(E) = \sum_{n,k} \left| \left\langle nk \left| \frac{\partial V_{ie}}{\partial \mathbf{R}_i} \right| nk \right\rangle \right|^2 \delta(E - \varepsilon_k + \varepsilon_F) \,. \qquad (13)$$

With the density functional method, the authors of [17, 18] calculated $N(0)\langle I_i^2\rangle$ for a number of systems, including aluminum. The calculation results for diamond and MgB_2 are shown in Figs 3 and 4 borrowed from [18]. As is seen in Fig. 3, the $\eta(E)$ function in doped diamond can reach rather high values if the chemical potential of the system is placed 6 eV below or 6 eV above that in pure diamond. The corresponding values of T_c can be rather high. For example, $T_c^{max} \approx 290$ K in the case of hole doping and $T_c^{max} \approx 420$ K in the case of electron doping. Unfortunately, it is still unclear whether it is possible to produce diamond with such a high level of doping. As regards high T_c, the situation in MgB_2 is much less optimistic (see Fig. 4). In Al, $N(0)\langle I_i^2\rangle$ very weakly depends on energy, and its absolute value is well below that for systems with covalent bonds.

Unfortunately, we cannot now unambiguously answer the question formulated in the title of this report. This is thought to be a dream rather than a myth. In 1976, Ginzburg published a note titled "High-Temperature Superconductivity: A Myth or Reality?" in *Physics – Uspekhi* [19]. Within almost a decade, this dream concerning high-temperature superconductors was achieved. We hope that the same will be true of room-temperature superconductivity.

Acknowledgments. I am grateful to V L Ginzburg for his constant support in studying the problem of high- and room-temperature superconductivity.

This work was supported by the state program for support of leading scientific schools, scientific programs of the Russian Academy of Sciences, and the Russian Foundation for Basic Research (project no. 08-02-00757).

References

1. Ginzburg V L *Phys. Lett.* **13** 101 (1964)
2. Little W A *Phys. Rev.* **134** A1416 (1964)
3. Cohen M L, Anderson P W, in *Superconductivity in d- and f- Band Metals* (AIP Conf. Proc., Vol. 4, Ed. D H Douglass) (New York: AIP, 1972) p. 17
4. Kirzhnits D A *Usp. Fiz. Nauk* **119** 357 (1976) [*Sov. Phys. Usp.* **19** 530 (1976)]
5. Anderson P W *Science* **316** 1705 (2007)
6. Maksimov E G, Dolgov O V *Usp. Fiz. Nauk* **177** 983 (2007) [*Phys. Usp.* **50** 933 (2007)]
7. Ogg R A (Jr.) *Phys. Rev.* **69** 243 (1946)
8. Bardeen J, Cooper L N, Schrieffer J R *Phys. Rev.* **108** 1175 (1957)
9. Schafroth M R *Phys. Rev.* **96** 1149, 1442 (1954); **100** 463 (1955)
10. Bednorz J G, Müller K A *Z. Phys. B* **64** 189 (1986)
11. Maksimov E G *Usp. Fiz. Nauk* **170** 1033 (2000) [*Phys. Usp.* **43** 965 (2000)]
12. Matsui H et al. *Phys. Rev. Lett.* **90** 217002 (2003)
13. Savrasov S Yu, Maksimov E G *Usp. Fiz. Nauk* **165** 773 (1995) [*Phys. Usp.* **38** 737 (1995)]
14. Maksimov E G, Savrasov D Yu, Savrasov S Yu *Usp. Fiz. Nauk* **167** 353 (1997) [*Phys. Usp.* **40** 337 (1995)]
15. Maksimov E G, Savrasov D Yu *Solid State Commun.* **119** 569 (2001)
16. Pickett W E *J. Supercond. Nov. Magn.* **19** 291 (2006)
17. Cohen M L *J. Supercond. Nov. Magn.* **19** 283 (2006)
18. Moussa J E, Cohen M L *Phys. Rev. B* **74** 094520 (2006); cond-mat/0607832
19. Ginzburg V L *Usp. Fiz. Nauk* **118** 315 (1976) [*Sov. Phys. Usp.* **19** 174 (1976)]

PACS numbers: **74.45.+c**, **74.78.–w**, **81.15.–z**
DOI: 10.1070/PU2008v051n02ABEH006466
DOI: 10.3367/UFNr.0178.200802f.0179

Experiments with atomically smooth thin films of cuprate superconductors: strong electron – phonon coupling and other surprises

I Božović

This paper is based on a presentation prepared for the Scientific Session of the Physical Sciences Department of the Russian Academy of Sciences held on October 4, 2007, in honor of 90th birthday of Academician V L Ginzburg. A short review is presented of our own work only, including some very recent experiments, on molecular beam epitaxy of thin films of high-temperature superconductors (HTS). We have developed a technique to fabricate HTS heterostructures with atomically smooth surfaces and interfaces. This has enabled a series of novel or improved experiments that

allowed us to address several key questions related to the physics of HTS such as how it relates to the proximal antiferromagnetic and pseudo-gap states. Firm experimental evidence is obtained that in HTS cuprates coupling of electrons to certain lattice vibrations is very strong. Next, we have observed interface superconductivity in bilayers consisting of two non-superconducting cuprates; the superfluid is confined within a $1-2$ unit-cell-thick layer next to the interface. In the long run, this discovery may revive the search for HTS in novel metal-insulator (MIMIM...) superlattices in which the mobile electrons in metallic layers are paired by interaction that is enhanced in or originates from the dielectric layers, as it was proposed by VLG forty years ago [1, 2].

1. The oxide molecular beam epitaxy (MBE) system at BNL

The experiments to be described in this review are based on advanced 'digital' synthesis technique whereby atomic layers of complex oxides are deposited one at a time, allowing for 'atomic-layer engineering' of the sample as needed for a particular experiment [3]. The enabling hardware is the 'next-generation' oxide MBE system (see Fig. 1) of our design and construction [4]. It is equipped with several state-of-the-art surface analytical tools that allow for unprecedented control of the film growth process based on *in-situ*, real-time, atomic-level monitoring of the film surface [4, 5]. Here we give a short description of this apparatus, now located at Brookhaven National Laboratory (BNL).

The main growth chamber (Fig. 1a) holds 16 spools ('arms'), each of which contains a metal atom source, a pneumatic linear-motion shutter, a gate valve and a turbo-molecular pump. It is thus possible to recharge, service, outgas or change each source without breaking the vacuum in the main chamber, even while a film is being grown. Conversely, it is also possible to valve-off all the sources, vent the main chamber, service whatever may be needed, pump the chamber down, and grow films later the same day. Because of this high level of modularity the system up-time (say, the fraction of time when it is possible to grow films) is essentially 100%, despite considerable system complexity. This performance is pretty much unique today among research-grade MBE systems and it has been the key 'secret' of the group's success.

For most elements, we use resistively heated thermal effusion sources (also called Knudsen cells, or K-cells for short), stabilized to a high level ($\Delta T = 0.1-1\,^{\circ}\mathrm{C}$). Depending on the element, we use K-cells of different type: low-temperature (for Ca, Sr, or Ba), standard (for Bi, Mn, Au), high-temperature (for La, Ti) or dual-filament (for Cu). The latter type allows one to keep the crucible lip hotter than the bottom, and thus to prevent the source material build up (with concomitant reduction in flux of evaporated atoms) near the top of the crucible. For refractory elements with the melting point too high for resistively heated effusion cells, we have special rod-fed electron-beam sources, made to match the K-cells in physical dimensions so that they are interchangeable. Altogether, with this variety of source types, we can cover most of the elements in the periodic table.

The growth chamber is also provided with a sample manipulator (6 degrees of freedom) that carries a sample holder equipped with four UHV-compatible quartz-lamp heaters, each of which is powered and controlled independently. The sample manipulator also supports a set of four water-cooled nozzles for delivery of ozone or another reactive gas.

A scanning quartz-crystal rate monitor (QCM) is mounted on a separate motorized and computer-controlled manipulator that allows for x, y, z motion. The deposition rate, for each source, can be mapped accurately over the wafer area.

The MBE machine also includes a custom-made 16-channel atomic absorption spectroscopy (AAS) system. Each AAS channel contains a hollow-cathode lamp matched to the source element, a mechanical chopper, fiber optics to guide the light to and from the source spool, a monochromatic filter, a photo-multiplier detector, a lock-in amplifier, an a/d converter, and supporting electronics. AAS allows us to accurately monitor the atomic fluxes in real-time (i.e., during film deposition). This capability is critically important to ensure the correct atom count, since due to exposure to ozone the evaporation rates of some source materials change substantially during growth. This is particularly the case for reactive metals such as Ca, Sr, or Ba that readily oxidize in ozone atmosphere, which causes the evaporation rates to drop. For this reason, we use AAS to monitor the atomic fluxes in real time and feed this information to the computer that controls the film growth. The corrections are implemented instantaneously by adjusting the shuttering times, while

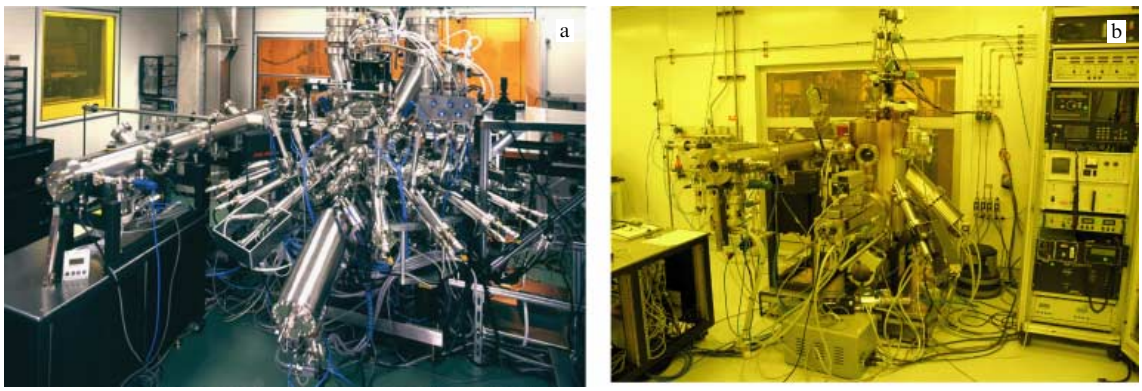

Figure 1. (a) The growth chamber of the MBE system at BNL is equipped with 16 metal atom sources, a pure ozone source (providing high oxidation power in high vacuum), a scanning quartz-crystal rate monitor, a 16-channel atomic absorption spectroscopy system, a scanning RHEED system, and a time-of-flight ion scattering and recoil spectroscopy system. (b) The processing chamber that allows for key lithographic steps (metallization, insulation, ion-milling, and ashing) to be done without breaking vacuum. It is located in a clean room which allows the substrates to be cleaned in a class-100 dust-free environment and loaded into the system for thin film deposition and processing.

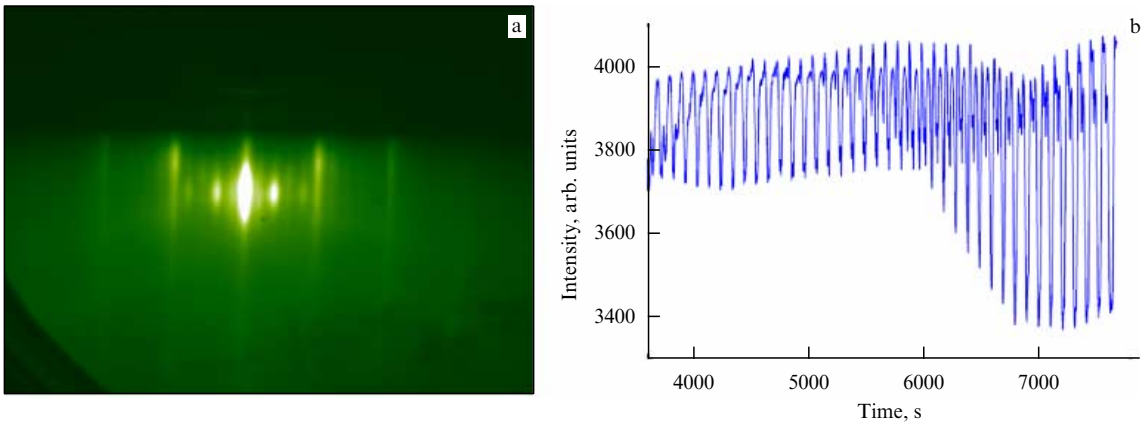

Figure 2. (a) A RHEED image from a thin film of $La_{2-x}Sr_xCuO_4$, viewed along the (100) crystallographic direction. The very bright spot near the center comes from the specular reflection. (b) RHEED oscillations during growth of this film. The intensity of reflectance is measured at the specular spot, as a function of time. The oscillations originate from periodic surface roughening and smoothing. The maximum reflectance is approximately constant, evidencing that the atomic smoothness of the surface is maintained as the film grows thicker. The beating comes from a small error in the absolute growth rate — the shutter opening time was not perfectly adjusted to deposit exactly one atomic mono-layer at a time.

the source temperature is kept constant to a high precision. This mode of operation provides for much better accuracy than the traditional one of adjusting the atomic fluxes by changing the source temperature, because the thermal response is much slower (and oscillatory). The 16 independent AAS channels, one for each source, can all of be operated simultaneously, since the wavelength filtering ensures that there is no cross-talk between different channels.

A Reflection High Energy Electron Diffraction (RHEED) system provides real-time information on the crystalline structure of the surface. A typical diffractogram is shown in Fig. 2a.

A Time-of-Flight Ion Scattering and Recoil Spectroscopy (TOF-ISARS) system is also integrated within the growth chamber. It provides quantitative information on the chemical composition of surface layers in real-time during film growth [5]. The principle of operation is as follows: a source of ions (e.g., K^+) provides a monochromatic ($E = 10$ KeV) beam, which is chopped by electrostatic steering. Each time the beam hits the collimator a bunch of ions makes it through and we monitor accurately their time of arrival at a multi-channel detector. The projectile ions hit the surface of the film and get scattered; one can measure their energy and momentum. This is called Ion scattering spectroscopy (ISS) and it is similar to the more familiar Rutherford backscattering spectroscopy (RBS), except that here the ions impinge at the surface with a low energy and at a nearly grazing angle. This provides for great surface sensitivity — we are probing only one or two top atomic monolayers. Some ions and neutral atoms are sputtered away from the surface, collected and mass-analyzed. This is called Direct Recoil Spectroscopy (DRS) and it provides information on the chemical composition of the surface. The TOF-ISARS apparatus built into our MBE system has four detectors at different angles, including a Mass Spectroscopy of Recoiled Ions (MSRI) analyzer. The later is supplied with a built-in automatic compensation for multiple scattering so that it can 'focus in time' the ions of the same mass irrespective of their energy and thus achieve the highest mass resolution — enough to resolve all the naturally occurring isotopes, see Fig. 3.

An important integral part of the MBE system at BNL is the processing chamber shown in Fig. 1b. It contains several

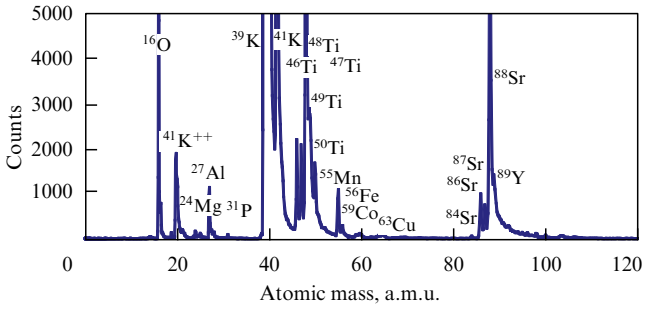

Figure 3. Mass spectrum of ions at the surface of a $SrTiO_3$ substrate obtained using the MSRI analyzer of TOF-ISARS system. The mass resolution is high enough to clearly identify the naturally occurring isotopes. This particular substrate was contaminated from exposure to a hot stainless-steel holder in a different chamber and all the contaminant ions can be seen. TOF-ISARS provides precious information on the chemical composition of the film surface, *in situ* and during film growth.

tools for lithographic operations: (i) a 5-pocket electron-beam evaporator, used to deposit metallization (usually Au, Ag, or Nb) and insulation layers (Al_2O_3, SiO_2, MgO), (ii) an oxygen plasma source for ashing photoresist residue and cleaning the surface *in-situ*, and (iii) a two-inch-diameter ion-beam source that enables lithographic features to be fabricated by ion milling. A liquid-nitrogen cooled, 6-degree-of-freedom sample manipulator allows for complex rotation patterns. The large-diameter, parallel ion beam makes it possible to fabricate deep trenches and other vertical lithographic features, as well as very shallow (low-angle) ramps. The processing chamber is located in a clean room; this allows the substrates to be cleaned in a class-100 environment and loaded dust-free into the system for subsequent film deposition and processing. The two chambers are connected by a 20-foot long transfer chamber that can maintain ultra-high vacuum on the 10^{11} Torr scale.

2. Atomically smooth HTS films grown by MBE

Leveraging on these advances in the apparatus and in the technique, we have succeeded in developing the technology for reproducible fabrication of atomically smooth films of cuprate superconductors and other related complex oxides

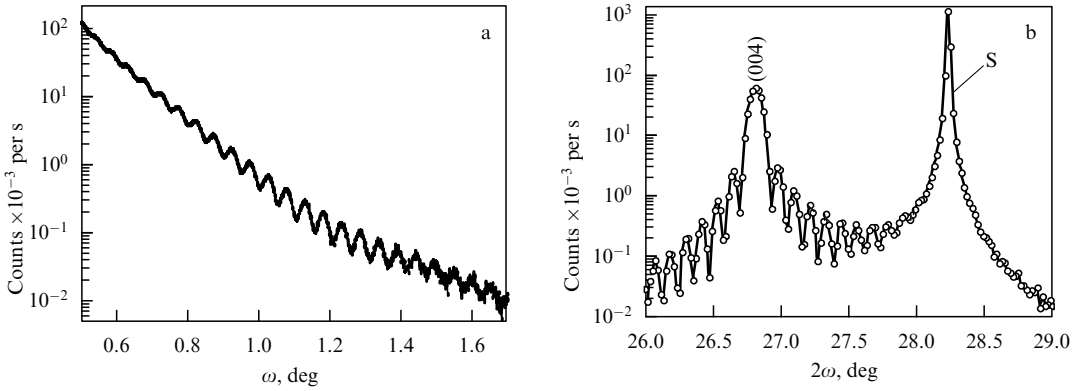

Figure 4. (a) Low-angle X-ray reflectance oscillations from a $La_{1.85}Sr_{0.15}CuO_4$ film, 78 nm thick, grown on top of a LaSrAlO4 substrate [4]. These oscillations are analogous to the Fabry–Perot interference between light beams reflected from two mirrors that are parallel and perfect on the scale of the wavelength of light. (Here, $\lambda = 1.54$ Å) (b) X-ray diffraction (the $\Theta - 2\Theta$ scan) near the (004) reflection from a $La_{1.85}Sr_{0.15}CuO_4$ film. Finite thickness oscillations are seen as side-bands to the strong Bragg reflections from the film and the substrate. The difference in angle between the two successive sidebands is determined by the total film thickness, while the position of Bragg peaks is determined by the lattice constant.

[5–8]. The key indicators are undamped RHEED oscillations observed during film growth, spectacular finite-thickness interference patterns seen in X-ray scattering, and flat, defect-free surfaces directly observed in scanning electron microscopy and atomic force microscopy (AFM) images.

In Fig. 2a we show a RHEED pattern observed from a very flat $La_{1.85}Sr_{0.15}CuO_4$ (LSCO) film during growth. Notice that the pattern is dominated by a very strong and sharp spot from the specular reflectance; this is an indication that the surface is very smooth. If we measure the reflectance intensity at this spot as a function of time, we observe regular oscillations such as seen in Fig. 2b. These oscillations come from periodic surface roughening and smoothing. The initial substrate surface is atomically flat. When the first layer is nucleated, the surface gets progressively rougher as the islands get more numerous. However, once that a half of the surface is covered, the reflectance starts increasing again as the islands grow in size and coalesce, until the layer is completed, at which point the reflectance reaches the second maximum. If the film growth is perfect, after each such cycle the surface should get atomically smooth again, and the reflectance maximum should not decrease with time. In contrast, a decrease in reflectance and damping of the intensity of oscillations is a signal of progressive roughening of the film surface as the growth proceeds. This is apparently not the case in Fig. 2b; indeed, in many instances, we have observed the maximum RHEED intensity to increase with the film thickness. On occasion one can discern beating, i.e., the presence of the second, much longer period in RHEED oscillations, as seen in Fig. 2b; this indicates a small error in the absolute calibration of deposition rates, which can be evaluated from such a graph and corrected subsequently.

In Fig. 4a, we show the X-ray reflectance measured at very low (nearly grazing) angles from a very flat LSCO film grown by MBE. Pronounced oscillations are seen in the intensity as a function of the angle of incidence. This is analogous to Fabry–Perot fringes that result from interference between the light beams reflected from two mirrors. Fabry–Perot oscillations are pronounced only if the two mirrors are parallel and perfect on the scale of the wavelength of light employed. Here, the wavelength of the X-ray radiation is 1.54 Å. In Fig. 4b we show the standard $\Theta - 2\Theta$ diffraction pattern taken at a larger angle from a similar film. Apart from the very strong Bragg reflections that originate in diffraction from the film and the substrate, one can see pronounced sidebands, the so-called finite-thickness oscillations. The separation between the Bragg peaks is determined by the film lattice constant, while the difference in angle between the two successive sidebands is determined by the total film thickness. This is essentially the same phenomenon as what is shown in Fig. 4a; the interference occurs between the X-rays reflected from the film surface and from the film/substrate interface. Indeed, this indicates that the two surfaces are flat and parallel to one another on the Å length scale.

In Fig. 5 we show an AFM image of a LSCO film grown on a $SrTiO_3$ substrate by MBE. Apparently the film is atomically flat, except for some one-unit-cell tall steps. These originate from the substrate; the commercially available ones are never polished exactly at the desired crystallographic plane but rather miscut by 0.1–0.5°. This generates few hundred angstroms wide terraces at the substrate surface that are typically separated by one-unit-cell tall steps. This causes occurrence of similar steps and terraces at the surface of growing film. Nevertheless, in the film shown in Fig. 5, the rms surface roughness over the area as large as 2,500 μm^2 was no more than 2–3 Å. This is essentially a single atom height, definitely much less than the 1 UC height, which in LSCO is $c_0 = 13$ Å.

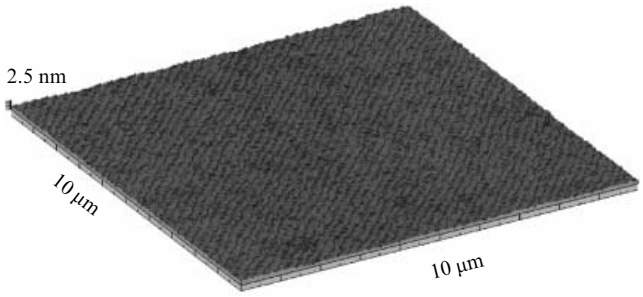

Figure 5. Atomic force microscopy image of a $La_{1.85}Sr_{0.15}CuO_4$ film, 78 nm thick, grown on top of a $LaSrAlO_4$ substrate [4]. It shows terraces, about 300 nm wide, between one-unit-cell-tall steps, as a consequence of the slight (0.1°) miscut of the substrate. The rms surface roughness of this film was less than 0.3 nm – essentially just a single atom height and much less than the unit cell height, $c_0 = 1.3$ nm – over the area of 2,500 μm^2.

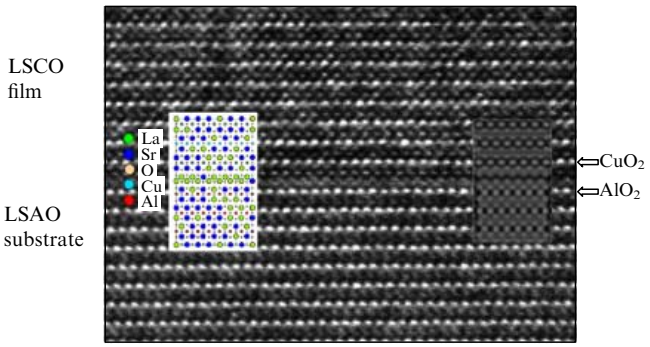

Figure 6. A cross-section image obtained by high-resolution Transmission Electron Microscopy (HR-TEM) of a $La_{1.85}Sr_{0.15}CuO_4$ film grown by MBE on $LaSrAlO_4$ substrate [9]. The micrograph shows formation of an unusual 'interface compound' — the sequence of reconstructed atomic layers that compensate for the polarization discontinuity at the interface. Knowledge and control of the right atomic-layer sequence is the secret of perfect hetero-epitaxy.

One important secret of perfect heteroepitaxy is the right sequence of atomic layers at the interface between the substrate and the film. If both are complex oxides, frequently one can observe formation of an interface layer of a third compound — sometimes a rather unusual one that does not exist in the bulk form. An instructive illustration is provided in Fig. 6 that shows an atomic lattice image of the interface between a LaSrAlO4 substrate and a $La_{1.85}Sr_{0.15}CuO_4$ film obtained by high-resolution transmission electron microscopy [9].

While atomically smooth HTS films were occasionally obtained in other laboratories, our group has been achieving this on a day-to-day basis. In the last year or so, the yield was essentially 100% (except for an occasional re-calibration growth right after we recharge the sources). This high yield of useful samples speeds up learning and enables fast progress. Thus it became possible to perform some unique experiments that are described in what follows.

3. HTS and the antiferromagnetic (AF) state

We have studied proximity effects between the HTS and the anti-ferromagnetic (AF) states, and found that they separate sharply, on the atomic scale [7]. The key piece of evidence is presented in Fig. 7. Trilayer junctions (Fig. 7a) were fabricated with HTS electrodes made out of LSCO ($T_c \approx 45$ K) and the insulating barrier consisting of just a single unit cell thick La_2CuO_4 (LCO) layer. As seen in Fig. 7b, there was no observable supercurrent even in the largest (80 μm diameter) junctions. The difference between three families of curves comes from different junction cross section; the area scaling was excellent and so was the uniformity among the junctions of the same nominal diameter [7]. This illustrates well the perfection of atomic layering: a single unit cell (1UC) thick barrier has no pinholes over macroscopic area. Note that we have revisited these findings recently at BNL and reproduced them over a dozen times, without a single exception.

In terms of fundamental physics of HTS, the significance of the above result is that it shows that the HTS phase and its 'parent' AF insulator phase do not mix but rather phase-separate very sharply, on the length scale of 1 Å. This corresponds to the AF barrier height of about 1 eV. Hence, the two phases are not degenerate (or nearly degenerate) in energy contrary to what has been postulated in a class of theoretical models for HTS.

The above experimental finding also revealed that there was no depletion/accumulation of charge between the superconducting (LSCO) and insulating (LCO) layers. The fact that the charge carriers stay in the doped layers indicates that the Coulomb interaction must be poorly screened along the *c*-axis. The same conclusions follow also from the 'reverse' experiment, illustrated in Fig. 8: a superlattice containing 1UC thick HTS layers separated by thicker insulating LCO layers has a high T_c and a sharp superconducting transition.

Independent verification of these statements came from a nice set of materials-physics experiments performed by I Felner and his group [10] on La-Sr-Ru-Cu-O (Ru-1212, 1222, -2212) compounds. These materials are unusual insofar that they show simultaneously high-temperature supercon-

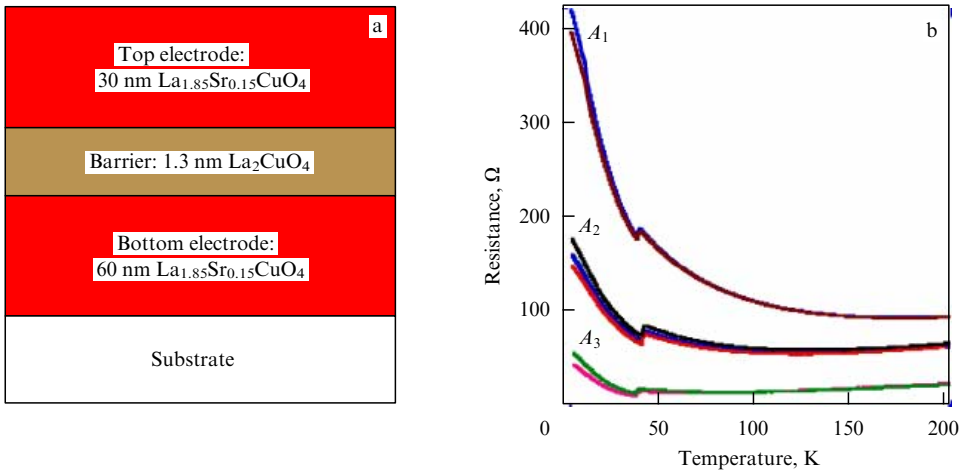

Figure 7. (a) A sketch of a trilayer SIS junction with one-unit-cell (1UC) thick LCO barrier. (b) The temperature dependence of resistance in three sets of such junctions with the mesa cross-section $A_1 = 1.8 \times 10^{-6}$ cm^2, $A_2 = 3.1 \times 10^{-6}$ cm^2, and $A_3 = 7.1 \times 10^{-6}$ cm^2, respectively [7]. Note that below ~ 40 K the LSCO electrodes and leads are superconducting and the voltage drops only across the LCO barrier. The absence of supercurrent and the high resistance seen even at the lowest temperature measured (4.2 K) indicate the absence of pinholes and shorts, but also that the LCO barrier height is substantial (about 1 eV).

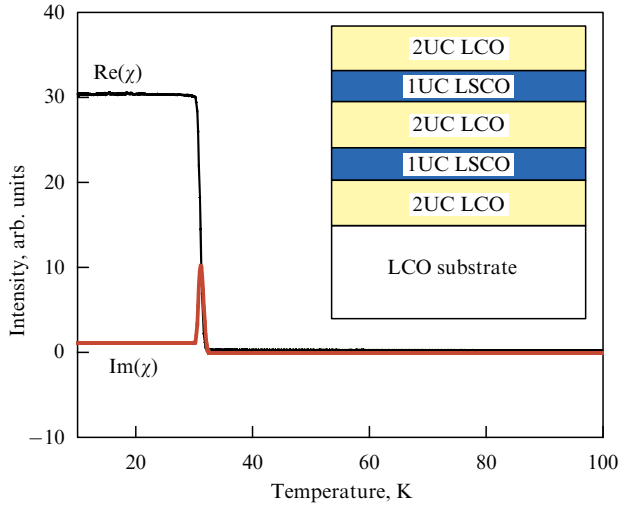

Figure 8. The temperature dependence of susceptibility (measured by the mutual inductance technique) of a superlattice film synthesized by alternating two-unit-cell thick layers of insulating La_2CuO_4 with one-unit-cell thick layers of $La_{1.85}Sr_{0.15}CuO_4$. Inset: the schematic structure of superlattice film [7].

ductivity with T_c as high as 40 – 50 K that resides in the CuO_2 layers, and antiferromagnetism with $T_N = 125-180$ K that originates from Ru magnetic moments. Felner et al. have demonstrated that T_c and T_N can be tuned independently of one another by site-selective chemical doping. In other words, HTS state is not influenced by the presence or absence of the AF state and v.v., even though the layers in which these states reside are separated by just few Ångstroms. Clearly, this would not be possible if the two states were degenerate and mixed over a large length-scale; in that case, one would only see a homogeneous mixture of the two. Given the experimental fact that the two states apparently do phase-separate on an extremely short length scale, it is not surprising that one can have in some samples many small or large islands of one phase in the matrix of the other phase, and be able to detect signals of their simultaneous presence. But this should not be confused with the two order parameters coexisting — i.e., existing in the same space at the same time as has been claimed in some papers. It is not obvious to the present author how a material could be an insulator and a superconductor simultaneously.

4. HTS and the pseudogap (PG) state

Next, we have studied proximity effects between the HTS and the so-called pseudo-gap (PG) state that is realized in underdoped cuprates. In stark contrast to the HTS-AF case, here we indeed observed [11] the so-called Giant Proximity Effect (GPE). When an underdoped layer is sandwiched between two optimally doped HTS layers, supercurrent can flow even through very thick 'barrier' layers.

In Fig. 9a, we have sketched a trilayer with the superconducting (S) electrodes made of LSCO with $T_c \approx 45$ K. The normal-metal (N′) barrier were made of underdoped $La_2CuO_{4+\delta}$ (LCO) with the typical $T_c \approx 25$ K and thickness $d = 200$ Å. The $I-V$ measurements were made as the function of temperature and we found that the devices behaved as SN′S Josephson junctions for $T_c' < T < T_c$. In Fig. 9b, we show how such a junction responds to microwave radiation ($\nu = 20$ GHz) at $T = 30$ K, i.e., above the T_c' of the barrier. One can see clear and sharp current jumps (Shapiro steps) at the voltages given by $nh\nu = (2e)\,V$, where $n = 1, 2, 3, \ldots$ This is clearly a *single* Josephson junction — there are no multiple voltage jumps characteristic of intrinsic junctions or a series of random weak links.

We believe that this GPE is genuine. In Ref. [11] we provided firm evidence that we have eliminated the key experimental hurdle in this field — micro-shorts, i.e., superconducting filaments connecting the electrodes. Our HTS trilayer junctions are free of any secondary phase precipitates and have atomically smooth interfaces — the rms surface roughness is much smaller than the barrier thickness. Further, we think that GPE is not the conventional S – N proximity effect. In our HTS-based SN′S junctions supercurrent flows across a barrier 100 times thicker than the superconducting coherence length, the mean-free-path of the charge carriers,

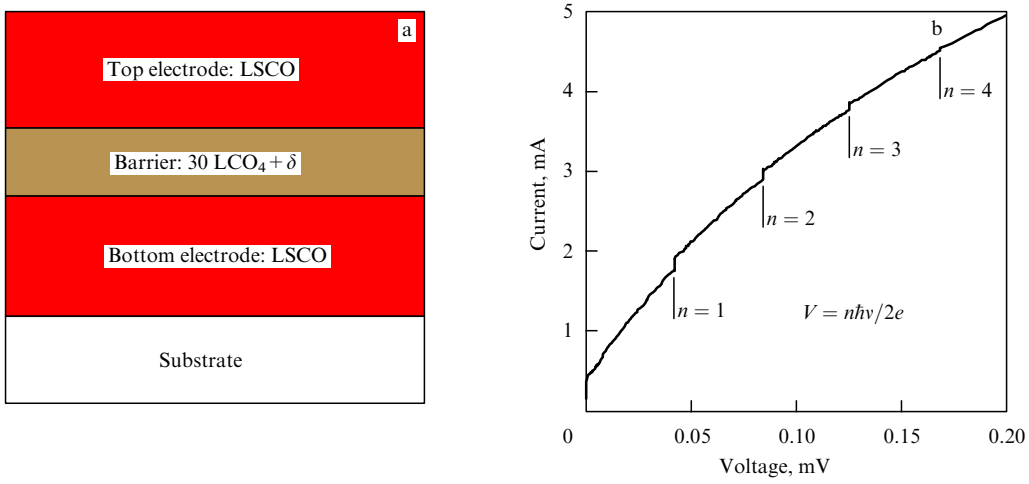

Figure 9. (a) (a) A schematic cross-section of a SNS trilayer junctions with the barrier thickness $d = 200$ Å. (b) The Shapiro steps induced in such a junction at $T = 30$ K (i.e., well above T_c of the N′ layer) by microwave radiation ($\nu = 20$ GHz) [11]. The steps occur at the voltages given by $V = nh\nu/2e$, for $n = 1, 2, 3, \ldots$, as expected for a single Josephson junction. This implies a 'Giant Proximity Effect' — the length scale is two orders-of-magnitude larger than what one would expect from the conventional theory and from the fact that both the coherence length in the HTS electrodes and the mean free path in the N′ layer are extremely short.

and the induced coherence length in N that one would have inferred from the conventional theory of the proximity effect. GPE may be the first really unconventional property of the *superconducting* state in the cuprates, and it imposes a new experimental constraint on the theory of HTS. We are continuing investigation of this effect at BNL, now using as the barrier underdoped LSCO with various level of Sr doping. So far the results seem consistent with our previous findings; hopefully we will be able to report some further advances before too long.

5. Interface Superconductivity

Superconductivity confined to nanometer-thick layers has been a long standing goal but very difficult to achieve. In ordinary metals the high electron density restricts carrier depletion and accumulation to a region much narrower then the superconducting coherence length. In copper oxides, the carrier density is low, the critical temperature high and the coherence length very short, so this provides a unique opportunity provided one can fabricate atomically perfect layers and interfaces. We have recently succeeded in fabricating virtually perfect heterostructures consisting of a metal ($M = La_{1.55}Sr_{0.45}CuO_4$) and an insulator layer ($I = La_2CuO_4$), neither of which is superconducting by itself — yet in the bilayers we reproducibly observe $T_c = 30$ K. By virtue of digital control of the layer thickness inherent to our atomic-layer MBE technique, we have established that in such heterostructures the HTS phase is confined within 1–2 unit cells from the interface. The detailed account of results, including the thickness and sequence dependence, the surface characterization by RHEED and TOF-ISARS etc., should be published soon [12]. One important finding is that interfaces appear to 'cross-talk' over large distances, as much as 500 Å — yet another indication that in cuprates the long-range Coulomb interaction is poorly screened along the *c*-axis.

We anticipate that the discovery of interface superconductivity will trigger further advances in several directions. For one, this makes reproducibly available robust ultra-thin HTS films, possibly including some with superconductivity confined to just a single CuO_2 plane. This should allow for a clean study of topological excitations such as vortex-anti-vortex pairs fluctuations in a 2D HTS gas. It may open the door to fabrication of practical three-terminal superconducting devices. Last but not least, this removes at least one important psychological barrier on the path to realization of Ginzburg's multilayer excitonic superconductor [1, 2]. We have demonstrated now that HTS can be sustained within a single unit cell layer, and that it can be influenced and enhanced across the interface from the proximal layer. The future will tell how far one can go using interface engineering to manipulate and control the inter-layer interactions.

6. Direct experimental evidence for strong electron-phonon coupling

Ever since the discovery of HTS in 1986, it has been a matter of heated debate whether coupling of charge excitations to the crystal lattice in cuprates is weak and essentially irrelevant or strong and crucial for the phenomenon. The opponents argue that there is essentially no oxygen isotope effect on T_c at optimal doping and hence no change in the ionic kinetic energy upon condensation, and that the electron–phonon coupling constant λ estimated from transport measurements or determined from *ab initio* band-structure calculations is small, $\lambda \approx 0.3$ in LSCO and $\lambda \approx 0.1$ in YBCO [13–19]. The proponents point out that a large (even too large) oxygen isotope effect is seen at other doping levels and in other physical observables (penetration depth, superconducting gap, pseudogap, effective mass, etc.), that large phonon anomalies have been detected in neutron scattering, and that tunneling spectroscopy shows phonon features coupled to the superconducting gap [20–31]. Other arguments, theoretical and experimental, abound on both sides of the divide.

Recently it has been discovered that intense short light pulses cause 'colossal' (larger then thermal) expansion in lanthanum cuprate films [32]. In this experiment, a thin LCO film was exposed to intense femtosecond (fs) light pulses. The evolution of crystallographic structure was monitored in real time by pulsed electron diffraction. The principle of the experiment is illustrated in Fig. 10a. The key result is shown in Fig. 10b: the c-axis lattice constant intermittently expands by as much as 0. Å. This lattice expansion is colossal if one compares it to the amplitudes of thermal lattice vibrations — the thermal expansion coefficient in LCO is 8.5×10^{-6} K^{-1}, so normally the crystal should have molten.

The fact that photo-doping induces colossal expansion implies very strong coupling of the lattice to charge-transfer excitations. This conclusion does not depend on theoretical modeling and follows essentially directly from the experimental data. Lattice expansion cannot come from magnons, plasmons, excitons, etc. More specifically, expansion along the *c*-axis can only come from *c*-axis *longitudinal acoustic phonons* (cLAPs). Strong coupling to cLAPs is unusual and characteristic of charged-layer superlattice structures; yet, it has been overlooked so far.

On the other hand, one can also conclude from rather general and detail-insensitive theoretical considerations [33] that the coupling to out-of-plane optic vibrations also must be strong. Generally, lattice expansion accompanies a reduction in crystal cohesion energy. In cuprates (and other related oxides) the cohesion is primarily of ionic origin and can be estimated as

$$U = \frac{e^2}{2} \sum \frac{q_i q_j}{|r_i - r_j|} + \frac{1}{2} \sum A_{ij} \exp\left(-B_{ij} |r_i - r_j|\right).$$

The first term is the Madelung energy (U_M); r_i and r_j denote the positions of the ions and q_1, q_j are their charges. The second term is the core repulsion energy modeled as the sum of nearest-neighbors repulsion terms in the standard Born–Mayer form. The sums are over all i, j with $r_i \neq r_j$. This simple framework accounts well for a range of properties — the cohesion energy, the charge-transfer gap, the crystal structure, the compressibility, and even the critical pressure for the orthorombic-to-tetragonal phase transition. It is convenient to fix the parameters A_{ij} and B_{ij} in such a way that the minimum of total energy coincides with the experimentally determined structure. Van der Waals interactions and covalency of the in-plane Cu–O bonds are included implicitly and are very small ($< 1\%$) terms anyway. Then one can allow for the (small) changes in q_i caused by chemical or photo-doping and predict the induced lattice distortions. We have tested how this model works in the case of chemical doping, where comprehensive neutron diffraction data have been reported and provide detailed information on the dependence of all atomic positions on the doping level x. We have found quantitative agreement without any fitting. To

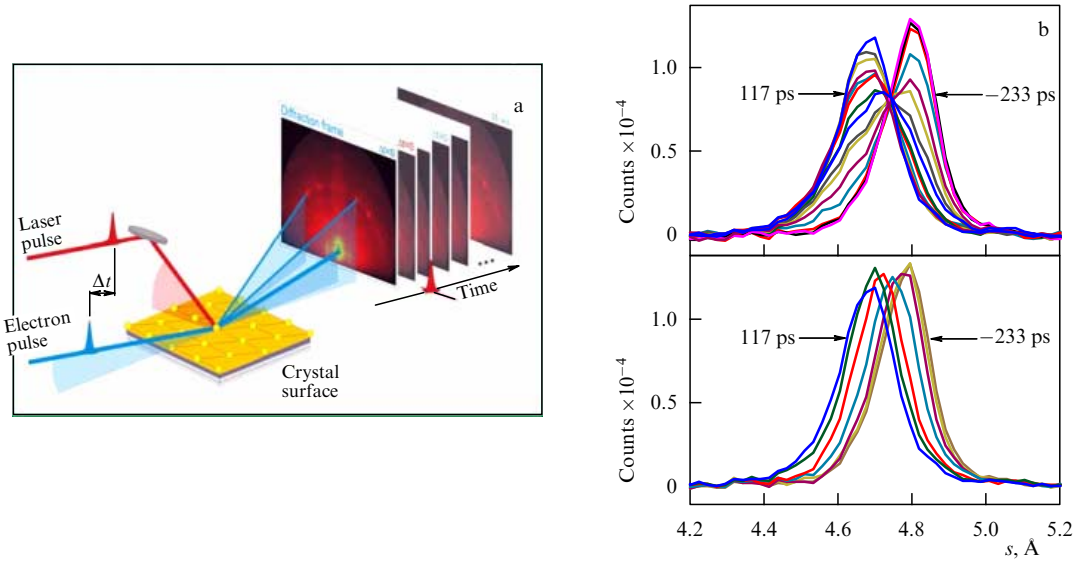

Figure 10. (a) Schematics of the ultrafast RHEED experiment of Gedik et al. [32]. An $La_2CuO_{4+\delta}$ film grown by MBE was photo-excited by intense short light pulses and the surface structure was analyzed using pico-second electron diffraction. By scanning the delay time one obtains RHEED 'movies' that show time-resolved changes in the crystal structure. (b) The main result: upon intense photo-illumination, the film expands along the c-axis by as much as 0.3 Å ($\sim$ 2.5%).

the first order, the ionic displacements are of purely electrostatic origin, i.e., just the consequence of the changes in ionic charges. Applying the same algorithm to photo-doping of epitaxially constrained films, we predict the *c*-axis expansion comparable to the one observed by Gedik et al., see Fig. 11. Moreover, the same simulation predicts significant intra-cell distortions, i.e., *c*-axis displacements of La and apical oxygen (O2) ions. In terms of the normal modes of the system, this implies strong coupling to two Raman active modes of A_{1g} symmetry, viz. vibrations of the La dumbbell at about 230 cm^{-1} and of the O2 dumbbell at 440 cm^{-1}.

The above conclusions may sound strange at the first glance. In the experiment of Gedik et al., the pump light beam was hitting the film with the electric field *parallel* to the CuO_2 planes, and yet we claim that this causes ionic motion in the *perpendicular* (out-of-plane) direction. In fact, this had been observed long ago but just overlooked. In Fig. 12, we reproduce Raman scattering data from Ref. [34]. The first panel (Fig. 12a) shows that the intensity of the apical-oxygen vibration mode at $\sim$ 500 cm^{-1} depends sensitively on the wavelength of the laser light. The second panel (Fig. 12b) shows in more detail how this intensity changes as a function of the photon energy, and compares this to the absorption coefficient in the material (for the same angle of incidence). The two spectral curves track one another; this is a clear indication of Resonant Raman scattering. The bizarre point (that even we missed ourselves in the original paper) is that the electric field of the light was *in-plane* and the ionic motion *out-of-plane*. A signature (anti-resonance) of *c*-axis phonons has been observed in *ab*-plane reflectance spectra as well [35]. Barring experimental artifacts, the only explanation I could think of is that the two subsystems, electrons and ions, are strongly coupled. If this is indeed the case, then if the mobile charges redistribute within the CuO_2 plane, the out-of-plane ions must move accordingly — and conversely, if these ions vibrate along the *c*-axis, this must cause a concomitant redistribution of the electron charge density within the CuO_2 plane.

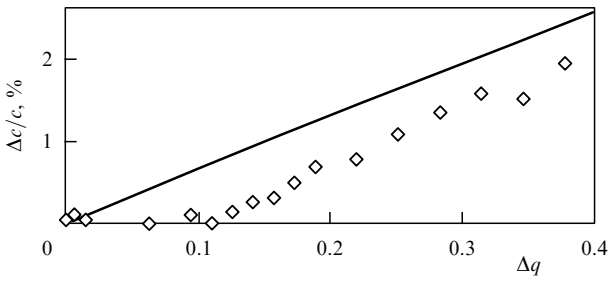

Figure 11. Colossal photo-induced expansion along the crystallographic *c*-axis in an MBE-grown $La_2CuO_{4+\delta}$ film: (◇) the experiment [32]; (the solid line) the calculations [33].

The root cause of this strong coupling is the Coulomb interaction which is indeed poorly screened in the *c*-axis direction — the fact I knew ever since recording the first polarized reflectance spectra of $YBa_2Cu_3O_7$ (YBCO) and $Bi_2Sr_2CaCu_2O_8$ (BSCCO) single crystals back in 1988–1989. In the *ab*-plane polarization, BSCCO looks like a metal (albeit a bad, over-damped one), but in the *c*-axis polarization it looks like the kitchen salt — there is no Drude peak, just strong dipole-allowed phonons. It took well over a decade before the (Josephson) plasma frequency along the *c*-axis in BSCCO was actually measured because it occurs in the microwave region — over an order-of-magnitude lower than the frequency of the optic phonons under discussion here.

The main problem here is that we expect the same effects to occur in other structurally and chemically similar ionic oxides. Indeed, some of these like e.g. $La_{0.5}Sr_{0.5}CoO_3$ and $Ca_{0.5}Sr_{0.5}RuO_3$ have infrared and Raman spectra (and other physical properties) quite alike to those seen in the cuprates [36]. However, none of these other oxides show HTS if they are superconducting at all. So clearly for HTS it is not enough that the electrons are strongly coupled to the lattice (including

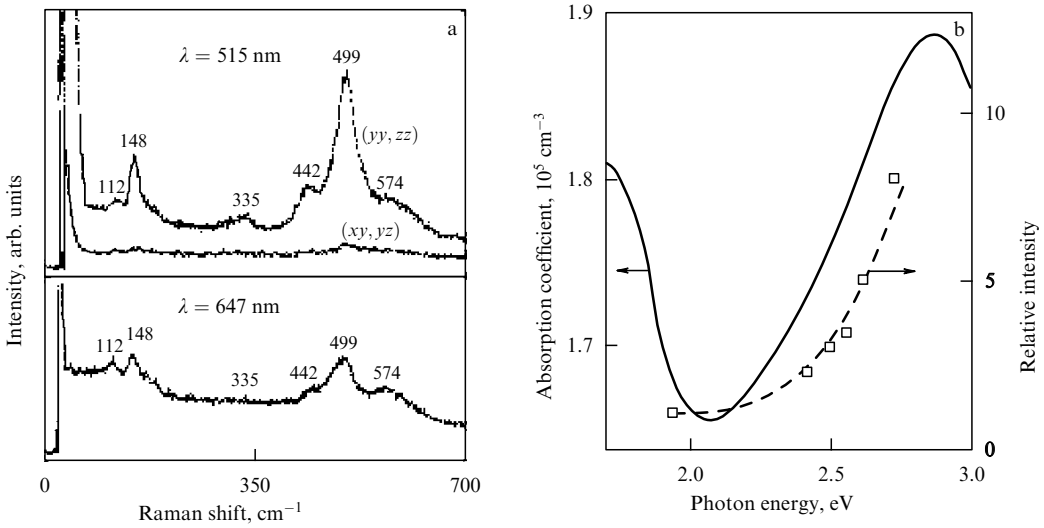

Figure 12. Raman scattering spectra of a $YBa_2Cu_3O_7$ film [33]. Note that the intensity of the strong feature at 499 cm^{-1}, the *c*-axis vibration of the apical oxygen, strongly depends on the wavelength of light. (b) A comparison of the intensity of this Raman-active mode to the absorption coefficient measured in the same sample as the function of photon energy [34].

the out-of-plane modes) — there ought to be something very specific to the cuprates that we are missing here. Many researchers in the HTS field believe that this uniqueness is in the strong electron correlations, spin 1/2, and the large $J \sim 0.13$ eV. However, even if this is the case, it seems to me hazardous to ignore the fact that in-plane charge excitations are strongly coupled to *c*-axis lattice vibrations — that *these excitations cannot be separated* — since they are ultimately responsible for both the normal state conductivity and HTS. In particular, if one wants to understand the doping phase diagram, one should be aware of the fact that between the undoped and optimally doped cuprates the Madelung energy may change by more then 1 eV *per atom* [33]. It is thus not surprising to see e.g. transfer of spectral weight in optical conductivity upon doping from the high-energy (1–2 eV region) to the Drude peak at low frequency [37], but it is hard to see how one could describe this using just a low-energy effective Hamiltonian.

7. Fingerprints of a polaronic metal

If indeed the electron – phonon coupling is very strong, at low density of doped charge carriers this should lead to small polaron formation and some sort of hopping transport with semiconductor-like temperature dependence. What to expect at a high doping density is less clear theoretically. Almost half-a-century ago T. Holstein speculated that at low enough temperature (when k_BT gets smaller then the polaron bandwidth) a 'polaronic metal' state with coherent transport should emerge [38, 39]. I am unaware whether this has ever been unambiguously observed in any material — and even whether it is a theoretically viable concept. On the other hand, if such a state existed I can say how it should look like to a spectroscopist.

Using the simplest possible toy model (classical and analytically solvable) of a non-interacting (Drude) gas of polarons one can indeed predict some unusual features in the optical spectra [40]. The reflectance should not show a sharp

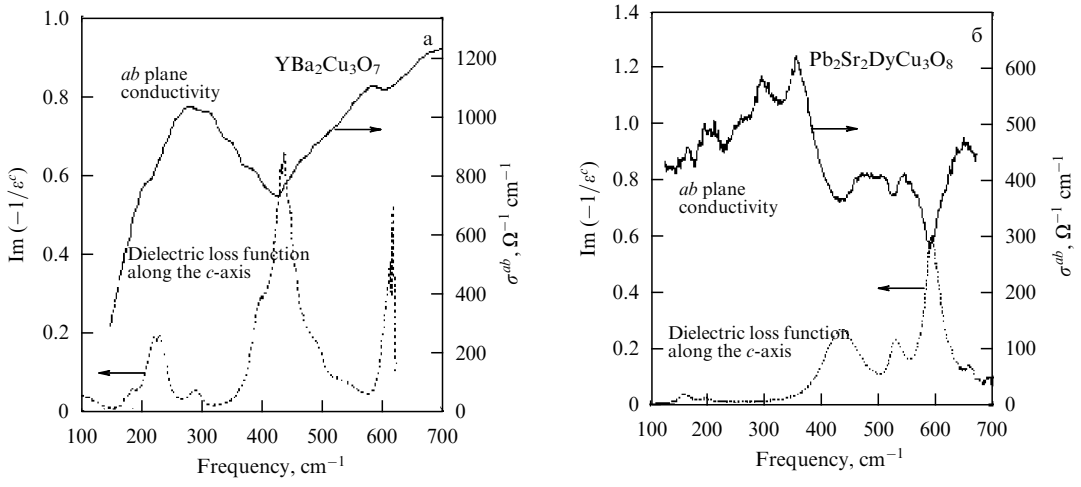

Figure 13. (a) The in-plane optical conductivity in $YBa_2Cu_3O_7$ shows minima that correspond exactly to the phonon peaks in the *c*-axis dielectric loss function; this may be indicative of strong coupling of out-of-plane phonons to the electrons in CuO_2 plane. (b) The same in $Pb_2Sr_2DyCu_3O_8$ [35].

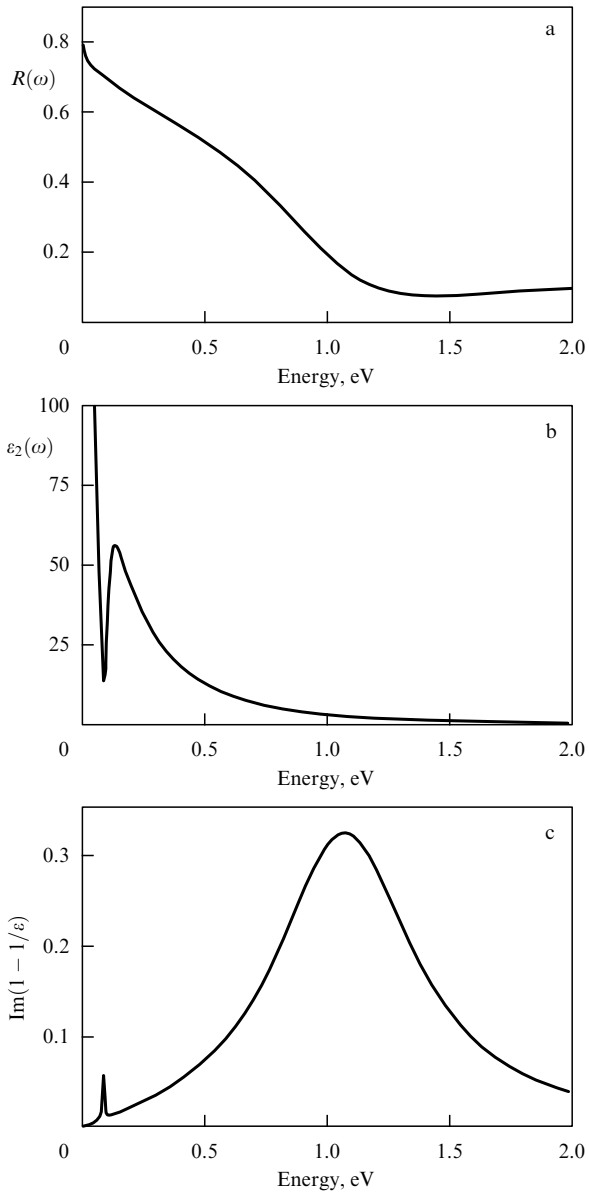

Figure 14. (a) The reflectance of a Drude gas of small polarons at high temperature. (b) At low temperature, the imaginary part of the complex dielectric function shows a pseudo-gap and (c) the dielectric loss function shows two distinct collective excitations, at high energy the usual plasmons and at low energy the longitudinal oscillations of the phonon 'clouds' [40].

plasma edge; at high frequencies well above the Franck–Condon ('undressing') transition the electron sees the large bare electron–phonon coupling and its motion gets overdamped, see Fig. 14a. More interesting things are expected to occur at low temperature and low frequencies: in the optical conductivity one would expect to see a pronounced minimum, something like a pseudo-gap, see Fig. 14b. This is related to the existence of second collective excitation in the polaron gas. At high frequency, there are plasma oscillations of essentially bare electrons. But since here we have an additional internal degree of freedom, i.e., the relative motion of the electron against its phonon cloud, there is a frequency at which the electrons don't oscillate (so there is no absorption) yet there are resonant longitudinal collective oscillations of the phonon 'clouds'. This excitation is not a plasmon, since it is charge-neutral. Neither is it a sound wave, since it is not acoustic — there is a finite restitution force. This prediction is not model-dependent — one should expect this from just counting the degrees of freedom. The new low-energy collective excitation should be observable at low temperature e.g. by high-resolution electron energy loss spectroscopy (HREELS) as a small sharp peak in the dielectric loss function, see Fig. 14c. This peak would be a clear fingerprint of the Polaron Metal — provided such an entity existed.

8. Conclusions

Based on our experiments with atomically smooth HTS thin films and heterostructures (multilayers, superlattices) we have concluded that HTS and AF states phase separate on Å scale while HTS and PG states mix over few orders-of-magnitude larger length scale. This indicates that HTS and AF states are well separated in energy while HTS and PG states must be almost degenerate.

Next, in such heterostructures we have observed interface superconductivity with a high T_c. It seems that HTS with the bulk T_c can be sustained in one-unit-cell thick cuprate layers. This discovery should have an impetus on studies of fluctuations in 2D superconductors as well as on HTS device physics. It also opens the field for study of HTS induced or enhanced by interactions and pairing across the interface, and putting to real test the decades-old prophecy of VLG.

Last but not least, picosecond diffraction experiments show colossal photo-induced expansion, which proves that there is strong coupling of in-plane charge excitations to *c*-axis acoustic phonons. Our model calculations indicate that out-of-plane optic phonons must strongly couple as well. We believe that this must be an important aspect of HTS physics in particular for understanding of the doping phase diagram.

More generally, we have shown that by atomic-layer engineering one can obtain unique samples and enable novel experiments to shed light on some basic physics problems such as the nature of HTS phenomenon.

Acknowledgment. The experiments at BNL were done in collaboration with G Logvenov, A Gozar, A Bollinger, and V Butko, and the numerical simulation in collaboration with Z Radovic and N Bozovic; their contributions were indispensable for the work reviewed here. I am also grateful for useful discussion and comments to V L Ginzburg, N Aschcroft, T H Geballe, M L Cohen, J C Phillips, J C Davis, J Zaanen, A Tsvelik, P Allen, and R Konik. This research has been supported by US DOE grant no. MA-509-MACA.

References

1. Ginzburg V L *Phys. Lett.* **13** 101 (1964)
2. Ginzburg V L *Zh. Eksp. Teor. Fiz.* **47** 2318 (1964) [*Sov. Phys. JETP* **20** 1549 (1965)]
3. Bozovic I, Eckstein J N, Virshup G F *Physica C* **235–240** 178 (1994)
4. Bozovic I *IEEE Trans. Appl. Superconduct.* **11** 2686 (2001)
5. Gozar A, Logvenov G, Butko V Y, Bozovic I *Phys. Rev. B* **75** 201402(R) (2007)
6. Bozovic I et al. *Phys. Rev. Lett.* **89** 107001 (2002)
7. Bozovic I et al. *Nature* **422** 873 (2003)
8. Abbamonte P et al. *Science* **297** 581 (2002)
9. He J et al. *J. Appl. Phys.* **101** 073906 (2007)
10. Felner I, in *Superconducting and Related Oxides: Physics and Nanoengineering V* (Proc. SPIE, Vol. 4811, Eds I Bozovic, D Pavuna) (Bellingham, Wash.: SPIE, 2002) p. 39
11. Bozovic I et al. *Phys. Rev. Lett.* **93** 157002 (2004)
12. Gozar A, Logvenov G, Bollinger A, Bozovic I (to be published)

13. Kapaev V V, Kopaev Yu V *Pis'ma Zh. Eksp. Teor. Fiz.* **68** 211 (1998) [*JETP Lett.* **68** 223 (1998)]
14. Belyavskii V I, Kopaev Yu V *Pis'ma Zh. Eksp. Teor. Fiz.* **73** 87 (2001) [*JETP Lett.* **73** 82 (2001)]
15. Belyavsky V I, Kopaev Yu V *J. Supercond. Nov. Magn.* **19** 251 (2006)
16. Leggett A J *Nature Phys.* **2** 134 (2006)
17. Zaanen J et al. *Nature Phys.* **2** 138 (2006)
18. Scalapino D J *J. Supercond. Nov. Magn.* **19** 195 (2006)
19. Anderson P W *Science* **316** 1705 (2007)
20. Ginzburg V L, Maksimov E G *Physica C* **235 – 240** 193 (1994)
21. Alexandrov A S, Mott N *Polarons and Bipolarons* (Singapore: World Scientific, 1995)
22. Zhao G-M et al. *Nature* **385** 236 (1997)
23. Müller K A *J. Supercond.* **12** 3 (1999)
24. Ginzburg V L *J. Supercond.* **13** 665 (2000)
25. Kulić M L *Phys. Rep.* **338** 1 (2000)
26. Abrikosov A A, in *Superconducting and Related Oxides: Physics and Nanoengineering V* (Proc. SPIE, Vol. 4811, Eds I Bozovic, D Pavuna) (Bellingham, Wash.: SPIE, 2002) p. 1
27. Ponomarev Ya G, Maksimov E G *Pis'ma Zh. Eksp. Teor. Fiz.* **76** 455 (2002) [*JETP Lett.* **76** 394 (2002)]
28. Maksimov E G, Dolgov O V, Kulić M L *Phys. Rev. B* **72** 212505 (2005)
29. Phillips J C *Phys. Rev. B* **71** 184505 (2005)
30. Lee J et al. *Nature* **442** 546 (2006)
31. Newns D M, Tsuei C C *Nature Phys.* **3** 184 (2007)
32. Gedik N et al. *Science* **316** 425 (2007)
33. Radovic Z, Bozovic N, Bozovic I *Phys. Rev. B* **77** 092508 (2008)
34. Kirillov D, Bozovic I, Char K, Kapitulnik A *J. Appl. Phys.* **66** 977 (1989)
35. Reedyk M, Timusk T *Phys. Rev. Lett.* **69** 2705 (1992)
36. Bozovic I et al. *Phys. Rev. Lett.* **73** 1436 (1994)
37. Uchida S et al. *Phys. Rev. B* **43** 7942 (1991)
38. Holstein T *Ann. Phys.* (New York) **8** 325 (1959)
39. Holstein T *Ann. Phys.* (New York) **8** 343 (1959)
40. Bozovic I *Phys. Rev. B* **48** 876 (1993)

PACS numbers: **74.62. – c**, **74.40. – b**, **74.78. – w**

DOI: 10.1070/PU2008v051n02ABEH006467
DOI: 10.3367/UFNr.0178.200802h.0190

Structural design of superconductors based on complex copper oxides

E V Antipov, A M Abakumov

1. Introduction

The design of new materials with important physical properties is one of the challenging problems of modern science. A variety of approaches are being developed in order to overcome labor-consuming exhaustive search of chemical compositions and synthesis conditions and to optimize the solution to this problem. Structural design is one of the most effective methods. This method involves an analysis of chemical composition – structure – property relations for a certain class of materials, possible structure types for a set of chemical elements that can be used to form the required crystal structure, the coordination environment of atoms in the structure, and the character of bonds between various atomic groups. Researchers from the Inorganic Crystal Chemistry Laboratory of the Chemical Department of Moscow State University used a structural design to search for new high-temperature superconductors based on complex copper oxides. In this report, we do not consider the crystal chemistry of high-temperature superconductors in detail. The main purpose is to describe the crystal chemistry principles of designing new superconductors that were used to fabricate new members of this unique family of materials and to predict ways to optimize their properties.

2. Structure and strategy of searching for new high-temperature superconductors based on complex copper oxides

Studying the relation between the composition, structure, and properties of numerous copper-containing high-temperature superconducting (HTSC) oxides has allowed formulating the following structural and chemical criteria required for the appearance of these properties:

(i) a layered structure in which (CuO_2) layers represent an infinite network of copper – oxygen CuO_4 squares connected by their vertices (Fig. 1);

(ii) optimum Cu – O interatomic distances in the layer plane (1.90 – 1.97 Å) to provide the overlapping of the $3d_{x^2-y^2}$ copper orbitals and the $2p_{x,y}$ oxygen orbitals with the formation of delocalized states in the σ^* band; and

(iii) an optimum carrier concentration in the (CuO_2) layers that corresponds to the formal copper oxidation state +2.05 to +2.25 for hole-doped superconductors and +1.8 to +1.9 for electron-doped superconductors.

Copper atoms can also be bound to oxygen atoms located in neighboring layers. However, these bonds are significantly longer and exceed 2.2 Å. Copper cations in the structures of superconductors have different chemical bonds with oxygen atoms: strong (planar) bonds in the (CuO_2) layer plane and much weaker (axial) bonds in the normal direction. The structures of the superconductors based on complex copper oxides are layered, and the framework structures of these oxides do not have superconducting properties.

Due to its negative charge, the (CuO_2) layer should be located between positive-charged or neutral cation – anion layers. Obviously, the most convenient layers are (AO) or ($A'\square$) (where $\square$ is an anion vacancy) layers. Figure 2 shows the (CuO_2) layer located between such layers in the two simplest structures, perovskite ABO_3 and $CaCuO_2$ (tetragonal anion-deficient perovskite structure). The structure (i.e., atomic positions and geometric characteristics) of this layer is optimum for the perovskite structure ABO_3, which contains layers of two types, (AO) and (BO_2), alternating along a fourfold axis. Therefore, all superconducting complex copper oxides have structures that are derivative of perovskite or contain a perovskite-like fragment as one of the structural blocks.

A complex oxide with a perovskite structure can be synthesized if the electric neutrality criterion is satisfied and the cation – anion distances correspond to the Goldschmidt

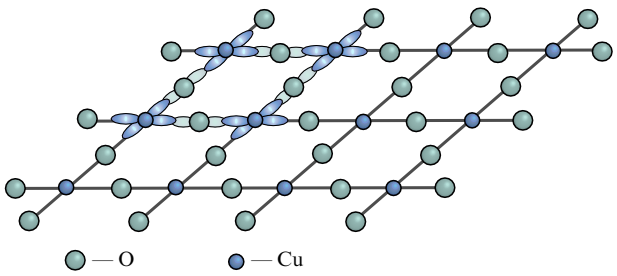

Figure 1. Structure of the copper – oxygen (CuO_2) layer.